

X-ray Based Craniofacial Visualization and Surgery Simulation

Junjun Pan, Jian J Zhang, Yanning Zhang, Hong Zhou

Abstract This paper presents a novel craniofacial visualization technique with the developments from both computer vision and graphics. It is a low radiation, low cost alternative to CT-based system for the reconstruction of 3D cranium using only three X-rays. We paste lead markers on the subject's face which allow a 3D face model to be constructed by correlated vision. Then the surface of the cranium is obtained by subtracting soft tissue depth from face surface. We also present a new algorithm to solve the matching by evolutionary programming and designed a supervised learning method to estimate the soft tissue stiffness parameters.

Keywords correlated vision; parameter estimation; surgery simulation; x-rays

1 Introduction

3D cranium reconstruction has received a lot of attention from both medical and computer graphics research communities, and is an effective approach for the visualization of the complex internal cranial structure. Existing methods acquire the raw image data by CT scanning, with which the volumetric geometry is reconstructed to produce a 3D computer graphics (CG) model of the head. They have been widely used in various medical visualization applications, including surgical planning, diagnosis and medical training.

Junjun Pan Jian J Zhang
National Center for Computer Animation, Media
School, Bournemouth University, UK
E-mail: pan_junjun@hotmail.com,
jzhang@bournemouth.ac.uk

Yanning Zhang
School of Computer Science, Northwestern
Polytechnical University, P.R. China
E-mail: ynzhang@nwpu.edu.cn

Hong Zhou
Stomatology Hospital of Xi an Jiao tong
University, P.R. China
E-mail: zhou57@pub.xaonline.com

Although it is justifiable to scan a subject by CT for serious diseases, such as tumour or accident-caused cranial trauma, the high dose of X-ray of CT scan can in many cases deter medical practitioners from taking advantage of the latest technology in computer graphics and visualization research. Taking orthodontic for young children as an example, CT scans are not very often used. One of the reasons is the X-ray dosage the subject receives. Statistics [1] suggests youngsters make up of about 80% of the patients in orthodontics and maxillofacial surgeries. And the x-rays dose from one CT head scan is approximately 20 times of the dose in one X-ray photographing. Large dose of X-ray radiation could have a serious adverse effect to the juvenile patient population. In addition, in comparison with ordinary X-ray photography (cephalometry), a CT scan is also more costly, which could be an issue for developing countries and underprivileged regions. In practice, ordinary X-ray photographing remains by far the most accessible and most commonly used medical imaging tool in craniofacial clinics. The technological advancement of 3D computer graphics has not been fully exploited in common medical practices. This is especially the case for orthodontics where the correction of the bony structure is usually followed and checked for years while the subject grows in age, as one would not like to subject the young patients with regular high dosage of X-ray radiation.

In this paper, we present a novel craniofacial visualization technique. Although at this stage, it remains a distance from being a clinically viable alternative, we hope this idea would merit further attention and development due to its unique advantages over the traditional X-ray based approach. We make three contributions in the paper. The first is a new craniofacial reconstruction technique combining the knowledge of computer graphics and computer vision. Instead of relying on a CT scan to acquire the internal structure of the head, we use only three ordinary X-ray photographs (cephalograms) together with an ultrasound scan. Compared with a full-blown CT scanning system, our technique

is able to produce a CG skull and the facial skin surface incurring only a fraction of the X-ray exposure to the subject. The second contribution is a new corresponding point matching algorithm that is able to identify corresponding feature points on different X-rays. In order to produce reasonably accurate simulation results, our third contribution is an easy-to-implement parameter estimation technique used with our finite element model (FEM) for the simulation of soft tissue deformations.

Human skulls and faces are of a free-form and complex shape. A small number of ordinary X-rays do not provide sufficient information for their geometry to be derived, owing to the penetration nature of X-rays. In order to overcome this problem, we stick a number of lead markers on the subject's face and take three X-rays photographs. The images of these lead markers on the three X-ray photos allow the face surface to be reconstructed once the correlated vision of the markers is established. The X-ray images we take display only the profiles of the skull. As they only record the accumulated density value of the tissues, not the geometry, three profiles curves of skull are far from enough for a detailed model to be rebuilt. Therefore, acquiring the facial skin surface is essential, not only for the evaluation of the appearance of the subject, but also for the reconstruction of the skull surface. With the subject's face model, we then derive the skull surface by subtracting the soft tissue thickness, which can be measured by M-ultrasound [2]. The profile curves of the skull, obtained by cephalograms, provide ground truth for the reconstruction, which is very useful to calibrate our calculations.

The simulation of soft tissue deformations has also attracted a great deal of research efforts and there exist a number of techniques. Two factors are important for the simulation accuracy, which are the mathematical model and the material parameters pertaining to the mathematical model. In this paper, we present a simple, but practical method for the estimation of the relevant simulation parameters, which are essential for enhancing the simulation accuracy. The estimated parameters are then used in our double-layered finite element model for the simulation of the soft tissue deformations.

This paper is structured as follows. After a brief introduction of the related work in Section

2, in Section 3 we describe our X-ray based craniofacial reconstruction and visualization technique including our new point matching algorithm. The simulation model and a stiffness parameter estimation technique are discussed in Section 4. Section 5 introduces the developed prototype system. Section 6 explains the experiments to study the accuracy and effectiveness of the approaches. We discuss the limitations of our system and future improvements in Section 7.

2 Related work

There are many craniofacial measurement and analysis methods, each has advantages and disadvantages and is appropriate for certain applications. In modern medical imaging, tomography, such as CT or MRI, represents the dominating technology in the reconstruction of the cranium with high accuracy [2, 3]. Recently, research on 3D craniofacial visualization and surgical simulation using both CT and laser scanning techniques has gained a popularity, which achieves high accuracy in the measurement of both soft tissue and bony structures [4~6, 23]. Reconstructing a head model using CT scans is relatively trivial, which can be undertaken with various volumetric graphics packages [1]. Because of the complexity of the human head structure and tissue behaviours, accurate simulation of tissue deformations proves very challenging. Many techniques have been explored by the research community with a varying degree of success. The typical deformation models include the finite element (FE) simulation [5, 6], mass spring systems (MSS) [7] and the Chain-Mail technique [8]. Among them, the FE models are likely to produce the best simulation accuracy, albeit its dependency on parameters setting. The advantage of the Chain-Mail algorithm is its ability to achieve a very high computational efficiency.

Although CT imaging produces high accuracy, some crucial factors, such as radiation and cost of the equipment, are of a concern to its applications. Some Japanese and Chinese medical institutes have realized this issue and made an effort to develop 3D cranium analysis methods from multiple orthodontic X-rays [9]. It works by manually selecting a set of feature points on the X-ray images and calculating the 3D coordinates

of them resulting in a craniofacial measurement. However, this system can only measure the given feature points and is unable to build a 3D cranium model. Laser scanning and structured lights are other effective non-invasive methods in the reconstruction of 3D human faces. However, they cannot measure the depth of soft tissues. If combined with X-rays, both types of the images have to be correctly registered, which is another tough problem in medical image processing.

3 Reconstruction of face and skull

X-ray imaging belongs to the penetrating projection imaging model. Each pixel on the image plane integrates the density of all the voxels through the line of sight. This means that an X-ray image does not offer any 3D surface or geometry information. Because of this, one is not able to derive a full geometric model from only a small number of X-ray photos, unless a full CT scan is used. But X-rays are very useful to identify boundary curves, which are useful for calibration as can be seen below.

Instead of trying to model a skull from X-ray photos directly, we endeavour to identify the skull surface starting from the face geometry. We use three X-ray photos for the purpose of both reconstructing a face surface and providing a datum for skull modelling [10]. X-rays penetrates both soft and hard tissues, but not the metal lead. This makes the lead marker points visible on the X-ray photos, which are placed on the face of the subject. We calculate the 3D position of each lead marker using correlated vision. The details of our point matching technique are given below.

Our technique consists of five steps: (1) enhancing images for easy detection of the pixels associated with markers. (2) identifying a feature region on the X-ray images; (3) matching corresponding feature regions on different X-ray images; (4) reconstructing a face model based on the computed 3D coordinates of all markers; and (5) derive the skull surface by subtracting the soft tissue thickness that is measured with M-ultrasound scanning.

3.1 System structure

The structure of our craniofacial visualization and simulation system is illustrated in Figure 1.

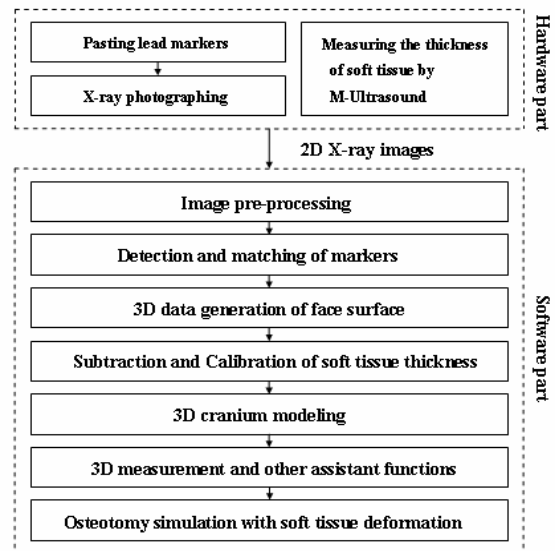


Figure 1 Structure of X-rays based craniofacial visualization and surgery simulation system

To produce the face model for a subject, we first paste a number of lead markers on the face of the subject, which are fixed on an adhesive tape beforehand. In our experiment, the lead markers are placed in a 30×15 matrix for half a face. We then fix the subject's head in the cephalometer in order to satisfy the requirements of the correlated vision. Experiments show that the optimal projection orientations are 0° (frontal), 60° and 90° (lateral) because of the least occlusion. We take three X-ray photos from these orientations. The X-ray images of 60° and 90° are used to reconstruct the 3D face model because of the least occlusion, and those of 0° and 90° are used to measure the thickness of soft tissue and calibrate and fine tune the M-ultrasound scanning data. To derive the accurate thickness of the soft tissue, the technician marks the approximate location of key markers on the skin by crayon after the adhesive tape is removed. The soft tissue thickness is measured using M-ultrasound, probing on the marked points on the face. The whole process usually takes five to six minutes. It is inevitable that errors are likely to be introduced from the manual operations. However, the two calibrating X-ray images taken at 0° and 90° provide accurate profile curves of the skull. This step allows the M-ultrasound measurements to be calibrated and errors minimized.

To maintain reconstruction accuracy, the maximum horizontal distance between two adjacent lead markers is confined to be 5mm, and the maximum vertical distance 10mm. Figure 2

shows a sketch of the X-ray photographing process.

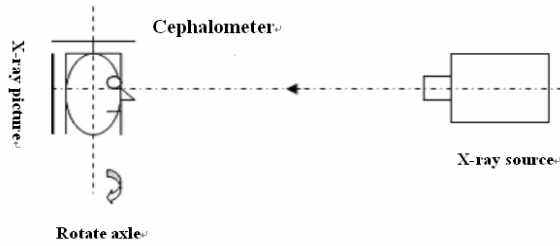


Figure 2 X-ray photographing with cephalometer

3.2 Surface imaging and feature points recognition

Two original X-ray images are shown in Figure 3.

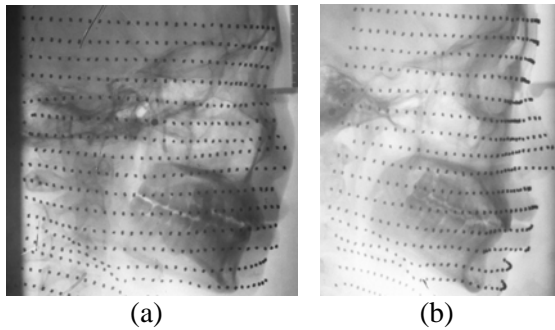


Figure 3 Original X-ray images pair. (a). 60° projection, (b). 90° projection

After histogram equalization, a following high-pass filter mask is designed to enhance the contrast of the isolated regions (the marker regions).

$$\begin{bmatrix} -5 & -3 & -1 & 1 & -1 & -3 & -5 \\ -3 & 0 & 1 & 2 & 1 & 0 & -3 \\ -1 & 1 & 2 & 4 & 2 & 1 & -1 \\ 1 & 2 & 4 & 8 & 4 & 2 & 1 \\ -1 & 1 & 2 & 4 & 2 & 1 & -1 \\ -3 & 0 & 1 & 2 & 1 & 0 & -3 \\ -5 & -3 & -1 & 1 & -1 & -3 & -5 \end{bmatrix}$$

Figure 4 gives the processed result. With the enhanced image, the feature points can be easily segmented by thresholding grey levels.

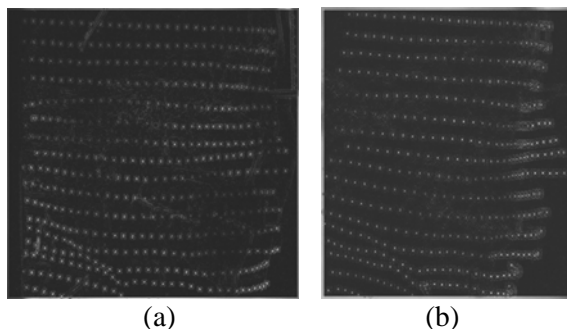


Figure 4 Image pair after feature points enhanced. (a). 60° projection, (b). 90° projection

To identify the image of a lead feature point on an X-ray photo, we designed a simple image recognition technique. Although numerous pattern recognition techniques exist, ours is intuitive and straightforward to use.

Our feature enhancing treatment above (Figure 4) has led to the arrival of a binary image, where each pixel has either a zero or one value. The feature region detection algorithm simply visits all pixels on a row-wise basis. A feature region on the image is identified if the value changes between adjacent pixels. In order to avoid the disturbance of image noise, a detected region is confirmed only if it spans at least a given number of pixels. We assume a region to be at least six pixels across in our experiments.

3.3 Corresponding points matching

Having detected the feature points, the next task is to match the corresponding points on two different X-ray photos to compute their 3D coordinates. Basically, a point pair should be searched along the same epipole line. This is a typical computer vision problem and there are many matching algorithms available [11~14, 19, 20], which can be mainly divided into two types: grey level based and geometric feature based. However, due to the penetrating projection nature of X-rays, neither of the two types is effective in this problem [15].

To tackle this issue, we present a new point matching algorithm, which is based on point position similarity, as described as follows:

In a correlated image pair, suppose there are n feature points in each image. Scan this image pair in the same order. During scanning, when a feature point is detected, its 2D coordinates are stored in a structure array. Scanning both images result in two arrays to be created containing the 2D coordinates of the feature points. Suppose the array for the first image is:

$$L\{l_1(x, y), l_2(x, y), l_3(x, y), \dots, l_{n-1}(x, y), l_n(x, y)\} \quad (1)$$

and that for the second image is:

$$R\{r_1(x, y), r_2(x, y), r_3(x, y), \dots, r_{n-1}(x, y), r_n(x, y)\} \quad (2)$$

For each feature point in one image, there is only one corresponding point in the second image regardless of the scanning order. This is a permutation problem and there are $n!$ different answers, among which only one is correct. Due to occlusion, markers may be missing from the images occasionally. But our experience didn't

find this poses a problem. The missing points can be easily added by the operator manually to make the total feature point number the same for both left and right images.

When the difference of the projection angles is small for both correlated images and the object, on which the feature points are placed, is largely convex, adjacent feature points have the same relative positions (or orders) on both images, i.e. they satisfy the ordering constraints in local region (The geometry meaning of the ordering constraints is: if $l_i(x, y)$ is a point in the first image and $l_j(x, y)$ is another point in the adjacent area of $l_i(x, y)$. Their corresponding points in the second image are $r_i(x, y)$ and $r_j(x, y)$. Suppose it exists $x_{l_i} \leq x_{l_j}$, $y_{l_i} \leq y_{l_j}$, then there will be $x_{r_i} \leq x_{r_j}$, $y_{r_i} \leq y_{r_j}$). Place both correlated images in the same coordinate system, and let the barycenter of feature points in both images coincide. Our proposition is that the summation of the Euclidean distance between pairs of corresponding points becomes minimised if the correct matching is found. The proof is given briefly in the Appendix. We call this algorithm the shortest distance matching based on position similarity.

Thus we have:

$$\min \sum_{i,j=1}^n d_{ij} \delta_{ij}$$

$$\mathbf{s. t.} \quad \sum_{j=1}^n \delta_{ij} = 1, i = 1, 2, 3, \dots, n,$$

$$\sum_{i=1}^n \delta_{ij} = 1, j = 1, 2, 3, \dots, n, \quad (3)$$

$$\delta_{ij} \in \{0, 1\}, i, j = 1, 2, 3, \dots, n,$$

$$d_{ij} = \sqrt{(x_{li} - x_{rj})^2 + (y_{li} - y_{rj})^2}, i, j = 1, 2, 3, \dots, n,$$

$\delta_{ij} = 1$ suggests the number i point in array L matches the number j point in array R . d_{ij} stands for the Euclidean distance between point i in array L and point j in array R . The objective function minimises the summation of the distances between two matched points. The two constraints represent that each point in one image should match only one point in the other image.

We solve this optimization problem by evolutionary programming. Using the reciprocal of $\min \sum_{i,j=1}^n d_{ij} \delta_{ij}$ to measure the fitness, the algorithm can be processed in the following steps: Making

L match R in sequence. Firstly we fix the sequence of the feature points in array L , change the sequence of two feature points in array R when there is a mutation operation in this position. Then calculate the fitness of each individual in new matching result, and eliminate the individuals whose fitness is small. The algorithm ends when a required tolerance (e.g. the difference of fitness) is reached leading to the identification of points matching. In the next section, we will compute the 3D coordinates of these marker points with stereoscopic method from which a 3D face model can be generated.

3.4 Coordinates computation and 3D face generation

Two rigid body transformations should be used in this step:

$$\begin{pmatrix} x \\ y \\ z \end{pmatrix} = \begin{pmatrix} x_l \\ y_l \\ z_l \end{pmatrix} + t_l \mathbf{R}_l \begin{pmatrix} x'_{l,i} \\ y'_{l,i} \\ F_l \end{pmatrix}, \quad \begin{pmatrix} x \\ y \\ z \end{pmatrix} = \begin{pmatrix} x_r \\ y_r \\ z_r \end{pmatrix} + t_r \mathbf{R}_r \begin{pmatrix} x'_{r,i} \\ y'_{r,i} \\ F_r \end{pmatrix} \quad (4)$$

\mathbf{R}_l and $(x_l, y_l, z_l)^T$ are the rotation matrix and translation vector for the left image (60° projection). Similarly, \mathbf{R}_r and $(x_r, y_r, z_r)^T$ are the rotation matrix and translation vector for the right image (90° projection). F_l (F_r) stands for the focal length of the left (right) image, t_l and t_r are two unknowns to be determined, which can be obtained by minimising d in (5).

$$d^2 = \left[\begin{pmatrix} x_l \\ y_l \\ z_l \end{pmatrix} + t_l \mathbf{R}_l \begin{pmatrix} x'_{l,i} \\ y'_{l,i} \\ z'_{l,i} \end{pmatrix} - \begin{pmatrix} x_r \\ y_r \\ z_r \end{pmatrix} - t_r \mathbf{R}_r \begin{pmatrix} x'_{r,i} \\ y'_{r,i} \\ z'_{r,i} \end{pmatrix} \right]^2 = [\mathbf{b} + t_l \mathbf{r}_l - t_r \mathbf{r}_r]^2 \quad (5)$$

Where \mathbf{b} stands for the basis of the world coordinates system. \mathbf{r}_l (\mathbf{r}_r) denotes the left (right) ray of sight rotated into the world coordinate system. Once t_l and t_r have arrived, the 3D coordinates of the feature point can be calculated using (4). The surface model is then trivially derived from the marker points. Figure 5 shows the 3D face model of the subject in experiment in Figure 3. Notice the reconstructed face model depends on where the markers are placed. As markers are not distributed, the eyes, eyebrows and hair cannot be modelled properly.

Fortunately, they are not necessary for the medical measurement we aim to.

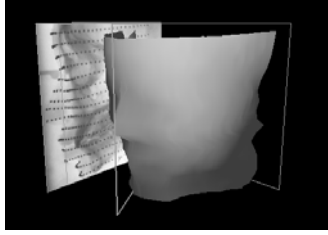


Figure 5 3D face model of a subject in experiment

3.5 3D cranium generation

From the obtained face model and using the thickness data by M-ultrasound scanning, we project the feature points inwards to derive the geometry of the skull. Generally, the resolution of X-rays is much higher than ultrasonograph. Therefore, to make the measurement more accurate, the M-ultrasonograph data need be normalized by the soft tissue depth in lateral and frontal X-rays (90° projection and 0° projection) first. This calibration process can be computed by following formula.

$$D_{i,j} = d_{i,j} \sqrt{\sin^2 \theta \left(\frac{D_{li}}{d_{li}}\right)^2 + \cos^2 \theta \left(\frac{D_{0i}}{d_{0i}}\right)^2} \quad (6)$$

Where $d_{i,j}$ is the original depth measured by M-ultrasonograph in the marker position of i -th row, j -th column. θ is the orientation angle in this position. d_{0i} , d_{li} respectively represent the original ultrasound measured depth in the position of the first and last markers at the i -th row. D_{0i} , D_{li} represent their corresponding depth in frontal and lateral X-rays. $D_{i,j}$ is the normalized depth. We assume the soft tissue thickness measurements were taken in the normal direction to the face skin surface. Figure 6 shows the 3D cranium surface model of the subject which is calculated from the face model shown in Figure 5.

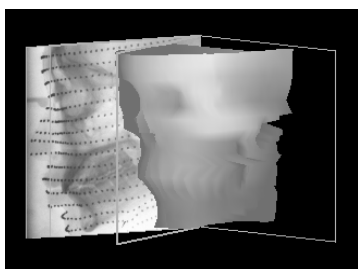


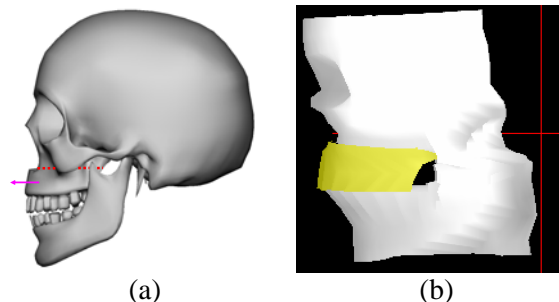
Figure 6 3D cranium model of the subject shown in Figure 5

4 Surgery simulation and soft tissue deformation

Once the skull and face models are generated, we can then implement a surgical simulation system. Soft tissue deformation is a complex phenomenon and its accurate simulation is of a practical significance. Many simulation models exist, which endeavour to approximate the soft tissue deformations as accurately as possible for virtual surgeries. Broadly speaking, there are two main physically based approaches, one is based on a finite element model (e.g. [5]), and the other one based on mass-spring systems [8]. Both FEM and MSS have had a varying degree of success in the simulation of soft tissue deformations. Since an accurate simulation proves extremely challenging due to the complex behaviour of living human tissues, all current techniques only attempt to approximate the behaviours.

Our FEM simulation method is not technically novel. Our contribution in this section is concerned with the formulation of the simulation parameters accurately. Here we briefly present our simulation model and discuss our supervised learning technique for the acquisition of accurate simulation parameters.

Before describing our soft tissue deformation and surgery simulation technique, let us first introduce some relevant medical background. Our study focuses on orthodontics, although the developed technique is applicable to other craniofacial visualization and simulation purposes. In orthodontics there are mainly two typical clinic abnormalities. One is known as the LeFort I, a kind of abnormality of the maxilla, which needs LeFort I pattern osteotomy. The other is the abnormality of the jawbone, which needs mandible vertical osteotomy. In Figure 7a and c, the red broken line illustrates the position and direction of bone cutting. Figure 7b and d show the operation simulation of these two typical osteotomies in our system.



(a)

(b)

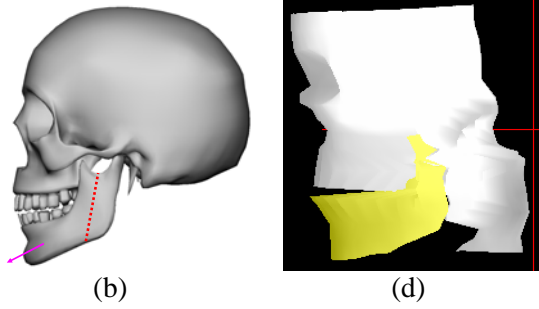


Figure 7 Two typical osteotomies and corresponding operation simulations. (a). LeFort I osteotomy, (b). surgery simulation of LeFort I, (c). mandible vertical osteotomy, (d). surgery simulation of mandible vertical osteotomy

To model the deformation behaviour of the soft tissues subject to surgical manipulations, we develop a double-layered non-linear, globally C^1 continuous finite element model for the face and cranium. The soft tissue forms the outer layer and the bone tissue is represented as the inner layer. It uses quadrangle polynomial shape functions similar to the modelling paradigm mentioned in [5]. Two material parameters, the modulus of elasticity (E) and Poisson's ratio (ν), are important for the simulation accuracy. Material properties vary from person to person and vary with the conditions of the person concerned, such as age, gender, ethnic origin and the environment they live in. This variation makes an accurate simulation model extremely difficult to come by. However, this issue appears to have been somewhat neglected in the literature.

In this research we hypothesize that the stiffness parameters are largely invariable in the local part of the facial surface for the same subject. Clinical practice suggests that facial deformities, such as the deformities for orthodontics, often require multiple corrective surgical interventions. In the following, we present an easy-to-implement supervised machine learning method to calculate the stiffness parameters based on some measurements obtained from the first operation. Although our hypothesis seems restrictive, it is very helpful for the planning and prediction of subsequent surgical operations, as multiple operations are often necessary in orthodontics. Our simulation technique based on the above presented cranial reconstruction technique gives the surgeon confidence in predicting the resultant outcomes with accuracy.

The training model adopts an iterative strategy, as given in (7) below. At the beginning, the

parameters are initialized with guess values. If available, one can use the parameters from other patients with similar conditions. After the computation of the soft tissue deformations using the above-proposed finite element model, the results are compared with the measured reference data (training data) taken from the operation. The errors are used to adjust the estimated parameters and this training process goes on until a predefined tolerance is satisfied. The training formula is given by

$$\varepsilon_{i+1} = \varepsilon_i + (T - t_i)k \quad (7)$$

where ε_{i+1} is one of the material parameters in step $i+1$ and ε_i is that at the previous iteration; T denotes the reference deformation in the training data set, which can be acquired from previous operations or related database; t_i is the current calculated deformation; k represents the training rate. In our experiments the training process is terminated when the difference between t_i and T is less than 0.3 mm. Given the trained parameters, we are able to predict the soft tissue deformations in our simulation case studies.

5 Prototype system

We have developed a prototype craniofacial visualization and surgery simulation system incorporating the above techniques. In addition, we have also implemented some auxiliary functions, one of which is a 3D metric measurement module. For completeness, here we give a brief introduction of this system.

Craniofacial surgeons often need to take measurements which allow them to diagnose, evaluate the conditions and appraise the outcomes of their surgical manipulations. This measurement is also necessary in order to acquire the training data (i.e. the measurement of certain distances). The derived skull geometry presented above makes an accurate measurement possible. From a practical point of view, such measurements can not be easily obtained without a 3D skull model. Without using our technique, one has to rely on CT scans to obtain the geometry of the cranium. Our X-ray based skull reconstruction technique can be used even in less well equipped cases. Using this 3D face and skull model, we implemented three types of measurement items: Euclidean distance, angles and geodesic distances which define the shortest

path between two points on a curved (skull) surface. The prototype system is developed with C++ and the OpenGL graphics library. Figure 8 gives a snapshot of the prototype system.

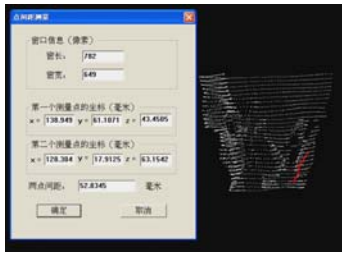


Figure 8 Measurement of various distances

6 Experiments and comparison

Our system was tested with three experimental case studies. The first is to test the accuracy of our points matching method and make a comparison with two other algorithms which are based on epipolar lines [19] and sequence matching [20]. Figure 9 shows the original X-rays pair. We placed 130 markers on the subject's right submaxillary. The comparison results are shown in Figure 10.

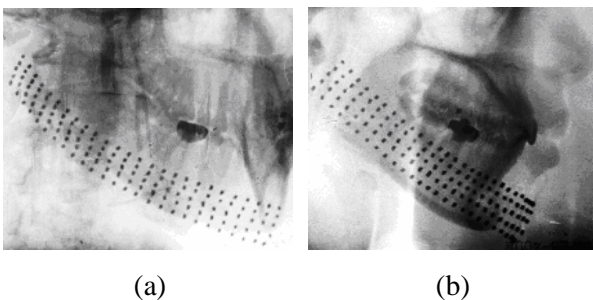


Figure 9 Original X-ray images pair. (a). 60° projection, (b). 90° projection.

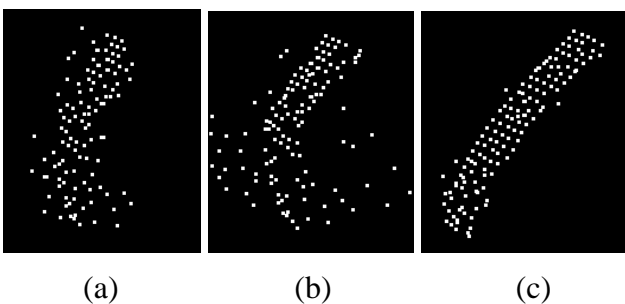


Figure 10 Results of corresponding points matching based on different algorithms. (a). 3D points matched by epipolar lines searching, (b). 3D points matched by sequence matching algorithm, (c). 3D points matched by our method

The 3D points in Figure 10a, based on epipolar line searches, show clear matching errors. The

reason is that the feature points are so dense that the error range is beyond the distance between two adjacent rows of feature points. In Figure 10b, as the limited adaptability of sequence matching algorithm, a number of points are badly mismatched. The result would be good if all points satisfy the ordering constraints, which is too strict to be practical. The result in Figure 3c, which is from our proposed matching method, demonstrates the best performance. In optimization searching by evolutionary programming, the generation scale number is $\frac{130(130-1)}{4} \approx 5000$. The time cost in whole process is 2.7 seconds and the accuracy of matching is 93.8%.

The second experiment is to test the accuracy of the 3D reconstruction technique. We compare the results with the data measured by a helical CT. Table 1 lists the results of some vertical items measured by our prototype system including Euclidean distance and geodesic distances in comparison with the CT imaging data. N, Gn, Sto, Sn stand for some facial feature points defined by the surgeon.

Table 1 Measurement errors (mm)

feature points	our system	CT	difference	permitted error tolerance
N-Gn	120.0	121.3	-1.3	± 2.7
N-Sto	86.0	83.3	2.7	± 2.9
Sto-Gn	35.42	38.4	-1.98	± 2.2
Sn-Go	60.69	60.9	-0.21	± 2.0
N-Sn	60.14	60.3	-0.16	± 2.6
Sn-Sto	26.33	24.8	1.58	± 2.6

Table 1 suggests that our cranial reconstruction technique and the developed system offer good modelling accuracy. All measurements are within the required tolerances. For certain items, the developed technique is almost as accurate as CT scans, which is encouraging. However, our technique suffers from some limitations. Because it formulates the face model using lead markers, it is not suitable for regions where lead markers can not be placed, for example, the areas covered by hair. The soft

tissue thickness measured by M-ultrasound is another source of inaccuracy.

The third experiment is designed to investigate the effectiveness and precision of the soft tissue deformation technique and our parameter estimation algorithm. The patient was undergone two osteotomy operations, Lefort I and mandible vertical osteotomy. In this experiment, the reference deformation data of Lefort I was taken, once the operation was complete and the measured data was used to train the Poisson's ratio (ν) for our double-layered finite element model. The trained parameter was then used to compute (simulate) the deformations incurred from the subsequent mandible vertical osteotomy. In our experiments, we fixed the value of the modulus of elasticity and only trained the Poisson's ratio, and we found one parameter sufficed. However, if both parameters need training, it is best to train them separately, i.e. to fix one while the other is being trained. Iterate the process until a predefined termination condition is met.

Using the trained Poisson's ratio $\nu = 0.463$, we ran our FEM simulation for the mandible vertical osteotomy. Figure 11 demonstrates the simulation results.

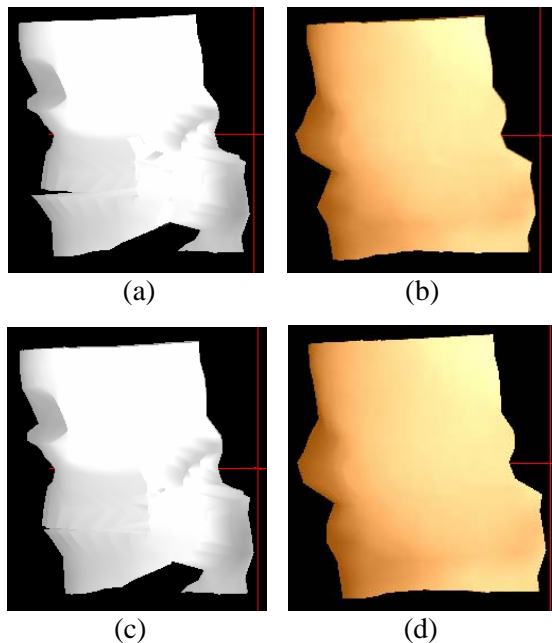


Figure 11 Mandible vertical osteotomy simulation. (a). bone tissue before surgery, (b). soft tissue before surgery, (c). bone tissue after surgery, (d). soft tissue after surgery

Table 2 Deformations in the mandible vertical osteotomy

regions	fang teeth	jawbone
Actual result	1.25:1	1.13:1
Simulation result	1.27:1	1.21:1

Table 2 shows the comparative results. According to the medical convention, the deformations are represented as a ratio of the bone tissue displacement and the soft tissue deformation. The comparison suggests that our simulation model coupled with the parameter estimation technique is capable of producing simulation results of good accuracy when both training and testing data are taken from a local region (e.g. the fang teeth region in Table 2). However, simulation errors may increase if the testing area is too far from the area where the training data is taken (e.g. the jawbone region).

7 Conclusions

We have presented an X-rays based craniofacial visualization and surgery simulation system using only three X-ray photos. Because X-ray imaging records the tissue density rather than its 3D coordinates, a small number of X-ray images do not give sufficient information for the reconstruction of the cranium of a subject. Unlike the traditional CT based approach, where the geometry is derived by evaluating the densities of the voxels, our first step is to formulate the face geometry using computer vision techniques. To reconstruct the skull, we measure the soft tissue thickness using M-ultrasound scanning data calibrated by lateral X-ray photos and subtract the tissue thickness from the face model.

In the step of corresponding points matching, we have developed a new algorithm by considering the similarity of the position sequences of the feature points. Our experimenting results show that our algorithm is able to overcome the difficulties of the existing techniques encountered with X-ray images.

The derived 3D geometry of the skull is valuable both for the simulation of soft tissue deformations and for the accurate measurement and evaluation of surgical results. Based on the obtained geometry of the face and the skull of a subject, we have implemented a craniofacial

simulation technique using a double-layered finite element model for the computation of soft tissue deformations. In particular, we have proposed a simple yet effective algorithm for the estimation of the material parameters, including Young's modulus and Poisson's ratio. This has proven crucial to the accuracy of the simulation.

Compared with the CT based craniofacial visualization approach, the primary merits of our technique are low radiation and low cost. It uses only ordinary medical equipment and therefore can be easily adopted in poorer and underprivileged countries and remote regions. We have conducted two surgical experiments, Lefort I and mandible vertical osteotomy. Practical measurements have shown that our craniofacial reconstruction technique produces small geometric errors, well within the required tolerance. The experiments also verified that our simulation technique, together with the parameter estimation algorithm, was of good simulation accuracy.

However, our development is at an early stage and has a number of limitations. The most obvious is that our current method for placing the lead markers is quite awkward and user-unfriendly. Nevertheless, our objective of this research is mainly to prove the research concept. The second is that it is not suitable for the areas that cannot be well represented by the lead markers, such as the places covered with hair. Therefore, it should not be considered to replace the CT system. The third disadvantage is that the simulation error may increase if the testing area is too far from the area where the training data is taken. But this is true for other existing simulation techniques as well.

The feedback from the doctors who participated in the experiments believed our method had unique advantages and was worth of further development. In future work, we will devise a new easy-to-use marker placement method to cover the patient face. Our idea is to design a special face mask to let the markers touch the face automatically, which can also guide the ultrasound scan with accurate placement of the probe. Using the developed prototype system, we also plan to investigate the relationship of the stiffness parameter values with human age, race, gender, ethnic origins and some other related factors.

References

1. Weimin F (2002) Orthodontics. People Hygiene Press, Beijing
2. Cuiling Z (2003) Engineering and clinic: modern medical imaging. Science and Technology Press, Shanghai
3. Fuchs J, Kacherie M (2000) System performance of multi-slice computed tomography. *IEEE Engineering in Medicine and Biology* **15**(3): 375-377
4. Jarjan Z, Pozzi J, Macelli F (1995) Optimization of scanning and processing parameters for the 3D reconstruction in computerized tomography of the facial bones. *Radiology Med* **89**(5): 578-585
5. Koch M, Gross H, Carls R, Buren F, et al. (1996) Simulation facial surgery using finite element models. In *Proceedings of SIGGRAPH 1996 Conference*, ACM Press, pp 125-132
6. Gladilin E, Zachow S, Deuflhard P, Hege H (2001) A biomechanical model for soft tissue simulation craniofacial surgery. International workshop on medical imaging and augmented reality (MIAR 01), pp. 137
7. Duysak A, Zhang J, Ilankovan V (2003) Efficient modelling and simulation of soft tissue deformation using mass-spring systems. In *Proceedings of the 17th International Congress and Exhibition on Computer Assisted Radiology and Surgery (CARS 2003)*, London; pp123-127
8. Gibson (1997) 3D Chainmail: a fast Algorithm for deforming volumetric objects. In *Proceedings of Interactive 3D Graphics Symposium 1997*; pp149-154
9. Vukooyami (2001) A useful method in the cranium measurement by X-rays. *Orthodontics Study* **12**: 1-2
10. Pan J, Zhang Y, Zhou H, David F (2005) 3-d Visualization System of the Cranium Based on X-ray Images, In *Proceedings of 9th International Conference on Information Visualization (IV2005)*. London, pp 71-76
11. Paul D, Tim H, Chris T, et al. (2000) Acquiring the reflectance field of a human face. In *SIGGRAPH 2000 Conference Proceedings*, ACM Press/Addison-Wesley Publishing Co, pp 165-172
12. Coppini R (2002) 3D knowledge driven reconstruction of coronary trees. *Med & Bio Eng & Compute* **29**: 535

13. Vladimir K (2003) Multi-camera scene reconstruction via graph cuts. PhD dissertation, Computer Science Department, Cornell University, Ithaca, New York, USA
14. Sylvain P, Francois X (2003) A surface reconstruction method using global graphic cut optimization. In *European Conference in Computer Vision*, Rhodes, Greece; pp 1-7
15. Pan J, Zhang Y (2005) Corresponding points matching based on position similarity. In *Proceedings of International Conference on Computer Graphics, Imaging and Vision (CGIV05)*, Beijing, pp 33-37
16. Enciso R, Alexandroni S, Benyamein K, et al. (2004) Precision, repeatability and validation of indirect 3D anthropometric measurements with light-based imaging techniques. *Biomedical Imaging: Macro to Nano. IEEE International Symposium 2004*, pp 1162-1167
17. Chai W, Sheng H, Sheng L, et al. (2001) Facial surgery simulation using finite element modelling. In *Proc. SPIE 2001*, Vol.4319, pp 608-614
18. Jin H, Xiaohan S, Xin L, et al. (2006) Geometrically-based potential energy for simulating deformable objects. In *Pacific graphics 2006*, Taipei, pp115-122
19. Gruen W (2001) Adaptive least squares correlation: a powerful image matching technique, In *Proceedings of International Conference of Remote Sensing 2001*. Phoenix, Arizona, pp 65-71
20. Jia Y (2000) *Computer Vision*. Science Press, Beijing
21. Adriana C, Joseph L. et al. (2003) Craniofacial applications of 3D laser surface scanning. *The Journal of Craniofacial Surgery* **14**(4): 449-455
22. Ki L, Hyeon H, Sean C et al. (2007) Effect of cephalometer misalignment on calculations of facial asymmetry. *Orthod Dentofacial Orthop* **132**(1):15-27
23. Aoki Y et al. (2001) Simulation of postoperative 3D facial morphology using a physics-based head model. *The Visual Computer* **17**(2): 121-131
24. Nakasima A et al. (2005) Three-dimensional computer-generated head model reconstructed from cephalograms, facial photographs, and dental cast models. *American Journal of Orthodontics and Dentofacial Orthopedics* **127**(3): 282-292

Appendix

In Section 3.4 we presented a proposition, which says that under the ordering constraint the summation of the Euclidean distance between pairs of corresponding points minimises if the correct matching is found.

Denote the known features on the image pair as $L = \{l_i = (x_i^{(l)}, y_i^{(l)})\}$ and $R = \{r_i = (x_i^{(r)}, y_i^{(r)})\}$, $i = 1, \dots, n$. From the ordering constraint, one holds that if $x_i^{(l)} < x_j^{(l)}$ then $x_i^{(r)} < x_j^{(r)}$; and if $y_i^{(l)} < y_j^{(l)}$ then $y_i^{(r)} < y_j^{(r)}$, $i \neq j$.

Therefore the shortest distance matching algorithm is described as:

$$\min_{(p, p')} \sum_i \|l_{p(i)} - r_{p'(i)}\|^2$$

, subject to the ordering constraint, where p, p' are denoted as the permutations of L and R respectively.

We need to prove that when the correct matching is found, the summation of the distances between matched feature point pairs is the minimum.

Proof: Assume that for the shortest distance solution, there exist two points A and B, whose projections on L and R are mismatched. For the correct match, one has

$$\|l_a - r_b\|^2 + \|l_b - r_a\|^2 = (x_a^{(l)} - x_b^{(r)})^2 + (y_a^{(l)} - y_b^{(r)})^2 + (x_b^{(l)} - x_a^{(r)})^2 + (y_b^{(l)} - y_a^{(r)})^2, \quad \text{while}$$

$$\|l_a - r_a\|^2 + \|l_b - r_b\|^2 = (x_a^{(l)} - x_a^{(r)})^2 + (y_a^{(l)} - y_b^{(r)})^2 + (x_b^{(l)} - x_b^{(r)})^2 + (y_b^{(l)} - y_a^{(r)})^2 \text{ is for the mismatching.}$$

Consider $(x_a^{(l)}, x_b^{(l)}, x_a^{(r)}, x_b^{(r)})$ on the x-axis. There are four distances as follows,

. Comparing $d_3^2 + d_4^2$ with $d_1^2 + d_2^2$ will yield two cases. One is that $d_1 + d_2 < d_3 + d_4 = (d_1 + \varepsilon) + (d_2 + \varepsilon) = d_1 + d_2 + 2\varepsilon$ ($\varepsilon > 0$), and the other is $d_1 + d_2 = d_3 + d_4 = c$. For the 1st one, one can yield $d_3^2 + d_4^2 > d_1^2 + d_2^2$. Thus, let's consider the 2nd one.

For a fixed length c with two variables $c = x + y$, let's consider $s = x^2 + y^2$. This leads to $s = c^2 - 2cx + 2x^2$. For this quadric function, one can observe that when x is becoming large or small (y is becoming small or large), s is becoming large. This implies,

$$\max^2(d_1, d_2, d_3, d_4) + \min^2(d_1, d_2, d_3, d_4) >$$

$\text{non max}^2(d_1, d_2, d_3, d_4) + \text{non min}^2(d_1, d_2, d_3, d_4)$. This suggests $d_3^2 + d_4^2 > d_1^2 + d_2^2$, that is,

$$|x_a^{(l)} - x_a^{(r)}|^2 + |x_b^{(l)} - x_b^{(r)}|^2 < |x_a^{(l)} - x_b^{(r)}|^2 + |x_b^{(l)} - x_a^{(r)}|^2.$$

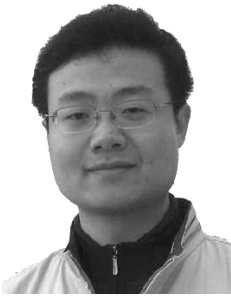
For $(y_a^{(l)}, y_b^{(l)}, y_a^{(r)}, y_b^{(r)})$, we hold the same conclusion. This implies that

$$\|l_a - r_a\|^2 + \|l_b - r_b\|^2 < \|l_a - r_b\|^2 + \|l_b - r_a\|^2.$$

It is clear that the solution is not a minimal solution. This conflicts with our assumption. We therefore conclude our proposition.

End.

Authors' biographies:



Junjun Pan is a PhD student in the National Centre for Computer Animation, Media School, Bournemouth University, United Kingdom. He received his bachelor (2003) and master degree (2006) in Computer Science from Northwestern Polytechnical University (P.R. China). His research interests include computer vision, medical visualization, virtual surgery simulation, and computer animation.



Jian J Zhang is a professor of Computer Graphics at the National Centre for Computer

Animation, Media School, Bournemouth University and Head of Research at Bournemouth Media School, United Kingdom. His research interests include computer graphics, computer animation, physically based simulation, geometric modeling, medical simulation and visualization.



Jian J Zhang is a professor in Computer Science School, Northwestern Poly-technical University (P.R. China) and Head of the Department of Computer Application and Engineering, IEEE member. Her research interests include image processing, pattern recognition, and computer vision.



Hong Zhou is a professor in Medical School, Xi'an Jiao Tong University and Vice-chancellor of Stomatology Hospital of Xi'an Jiao Tong University (P.R. China), the Senior member of Chinese Stomatological Association. His research interests include orthodontics, craniofacial plastic surgery, and craniofacial radiology measurement.